A Tryptophan that Modulates Tetrahydrobiopterin-Dependent Electron Transfer in Nitric Oxide Synthase Regulates Enzyme Catalysis by Additional Mechanisms†

Zhi-Qiang Wang, Chin-Chuan Wei, Jerome Santolini, Koustubh Panda, Qian Wang, and Dennis J. Stuehr*

Department of Immunology, The Lerner Research Institute, Cleveland Clinic Foundation, Cleveland, Ohio 44195

Received November 26, 2004; Revised Manuscript Received January 19, 2005

ABSTRACT: Nitric oxide synthases (NOSs) are flavo-heme enzymes that require (6*R*)-tetrahydrobiopterin (H_4B) for activity. Our single-catalytic turnover study with the inducible NOS oxygenase domain showed that a conserved Trp that interacts with H_4B (Trp457 in mouse inducible NOS) regulates the kinetics of electron transfer between H_4B and an enzyme heme−dioxy intermediate, and this in turn alters the kinetics and extent of Arg hydroxylation [Wang, Z.-Q., et al. (2001) *Biochemistry 40*, 12819−12825]. To investigate the impact of these effects on NADPH-driven NO synthesis by NOS, we generated and characterized the W457A mutant of inducible NOS and the corresponding W678A and W678F mutants of neuronal NOS. Mutant defects in protein solubility and dimerization were overcome by purifying them in the presence of sufficient Arg and H_4B, enabling us to study their physical and catalytic profiles. Optical spectra of the ferric, ferrous, heme−dioxy, ferrous−NO, ferric−NO, and ferrous−CO forms of each mutant were similar to that of the wild type. However, the mutants had higher apparent K_m values for H_4B and in one mutant for Arg (W457A). They all had lower NO synthesis activities, uncoupled NADPH consumption, and a slower and less prominent buildup of enzyme heme−NO complex during steady-state catalysis. Further analyses showed the mutants had normal or near-normal heme midpoint potential and heme−NO complex reactivity with O_2, but had somewhat slower ferric heme reduction rates and markedly slower reactivities of their heme−dioxy intermediate. We conclude that the conserved Trp (1) has similar roles in two different NOS isozymes and (2) regulates delivery of both electrons required for O_2 activation (i.e., kinetics of ferric heme reduction by the NOS flavoprotein domain and reduction of the heme−dioxy intermediate by H_4B). However, its regulation of H_4B electron transfer is most important because this ensures efficient coupling of NADPH oxidation and NO synthesis by NOS.

Nitric oxide synthases (NOSs)[1] are flavo-heme enzymes that catalyze a stepwise oxidation of L-arginine (Arg) to form nitric oxide and L-citrulline (*1*−*3*). In the first reaction, Arg is hydroxylated to form N^{ω}-hydroxy-L-arginine (NOHA), and in the second reaction, the NOHA intermediate is oxidized to form NO and citrulline (*4*). Both steps consume one molecule of O_2 and utilize NADPH-derived reducing equivalents. Three mammalian NOS isozymes have been characterized: neuronal NOS (nNOS, type I), mouse macrophage inducible NOS (iNOS, type II), and endothelial NOS (eNOS, type III) (*5*−*7*). Each NOS is only active as a homodimer (*8*, *9*). Their subunits are comprised of an N-terminal oxygenase domain, a C-terminal flavoprotein domain, and a central calmodulin binding motif (*9*−*11*). The oxygenase domain binds Fe−protoporphyrin IX (heme), the substrate Arg, and the essential cofactor (6*R*)-tetrahydrobiopterin (H_4B) (*12*, *13*), while the flavoprotein domain binds FAD, FMN, and NADPH (*14*−*16*). During catalysis, the flavoprotein domain provides electrons to the heme in the NOS oxygenase domain, which enables the heme to bind O_2 and initiate oxygen activation in both reactions of NO synthesis (*17*−*19*).

H_4B appears to have novel structural, redox, and electronic roles in NOS (*12*, *18*, *20*−*23*). For example, combined stopped-flow, rapid-quench, and rapid-freeze kinetic studies have demonstrated that H_4B transfers an electron to a heme−dioxy intermediate ($Fe^{II}O_2$) that is formed when O_2 binds to the ferrous heme in both reactions of NO synthesis (*17*, *18*, *24*). This is an important function for H_4B because the electron it provides enables the creation of the heme-based oxidants that react with Arg or NOHA (Scheme 1). Crystal structures of iNOS, nNOS, and eNOS oxygenase domain dimers (i.e., iNOSoxy) (*12*, *13*, *25*) showed that H_4B binds near the heme such that its 2-amino-4-hydroxypyrimidine

† This work was supported by National Institutes of Health Grants GM51491 and CA53914 (D.J.S.) and by grants from the American Heart Association (to Z.-Q.W. and C.-C.W.).

* To whom correspondence should be addressed: Department of Immunology NB-3, Lerner Research Institute, Cleveland Clinic Foundation, 9500 Euclid Ave., Cleveland, OH 44195. Phone: (216) 445-6950. Fax: (216) 444-9329. E-mail: stuehrd@ccf.org.

[1] Abbreviations: NOS, nitric oxide synthase; iNOSoxy, oxygenase domain of inducible nitric oxide synthase; nNOSoxy, oxygenase domain of neuronal nitric oxide synthase; Arg, L-arginine; DTT, dithiothreitol; NO, nitric oxide; EPPS, 4-(2-hydroxyethyl)-1-piperazinepropanesulfonic acid; NOHA, N^{ω}-hydroxy-L-arginine; H_4B, (6*R*)-5,6,7,8-tetrahydro-L-biopterin; Im, imidazole; CaM, calmodulin; FMN, flavin mononucleotide; FAD, flavin adenine dinucleotide; NADPH, nicotinamide adenine dinucleotide phosphate; Fe^{II}, ferrous species; Fe^{III}, ferric species; $Fe^{II}O_2$, ferrous heme−dioxy species. In referring to amino acids, we use the three-letter abbreviation, for example, Trp678. In referring to amino acid mutations, we use one-letter symbols to indicate the specific mutation, for example, W678A.

10.1021/bi047508p CCC: $30.25
Published on Web 03/05/2005

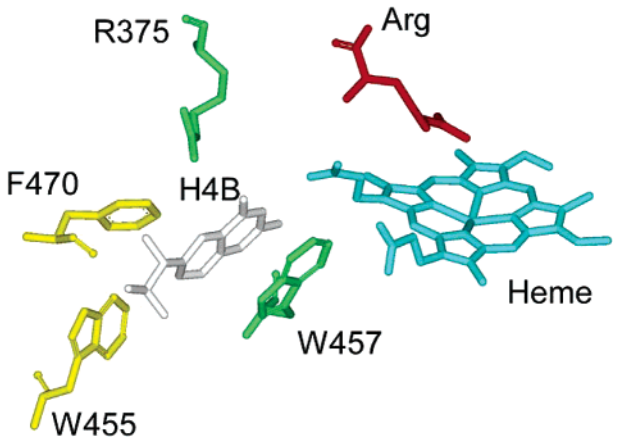

FIGURE 1: Residues whose side chains interact with the ring of H_4B. Green residues are provided by the same iNOSox subunit in which the H_4B is bound, and yellow residues are provided by the partner subunit of the dimer. Bound heme and Arg are indicated. This structure is based on the crystal structure of the mouse iNOSoxy dimer [PDB entry 1NOD (*12*)].

Scheme 1

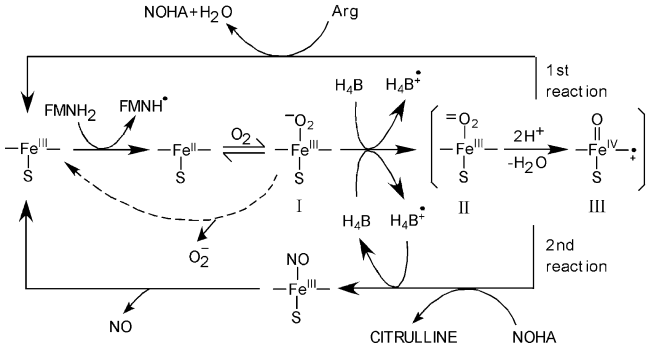

ring is hydrogen bonded with a heme propionate group (*26*, *27*). The H_4B ring also makes π-stacking and/or hydrogen bonding interactions with several conserved residues that are provided by both subunits of the NOSoxy dimer (Figure 1). Point mutagenesis has been used to probe the roles of these residues in modulating the functions of H_4B (*28*, *29*). This work has led to a particular interest in a conserved Trp (W457 in iNOS) that π-stacks and hydrogen bonds with the H_4B ring (Figure 1). Our previous studies showed that mutation of Trp457 to Phe and Ala weakened the dimeric interaction of iNOSoxy and decreased its affinity for H_4B and Arg (*28*). Moreover, single-turnover studies revealed that Trp457 controls the tempo of electron transfer from H_4B to $Fe^{II}O_2$ (*17*, *30*). This function appears to be important, because the slower rates of electron transfer found in the W457F and W457A iNOSoxy mutants were associated with proportionally slower and less complete Arg hydroxylation or NOHA oxidation in the single-turnover reactions (*17*, *30*). On the basis of these results, we proposed that slowing H_4B electron transfer might cause NO synthesis to become uncoupled in the full-length NOS enzymes. We have now tested this hypothesis directly using W457A iNOS and corresponding W678A and W678F nNOS mutants. By measuring a number of fundamental properties in these mutants, we found that their slower and uncoupled NO synthesis is primarily due to combined kinetic defects in electron transfer from H_4B and from the flavoprotein domain.

EXPERIMENTAL PROCEDURES

Materials. All reagents and materials were obtained from Sigma, Aldrich, Alexis, or sources described previously (*28*, *30*, *31*).

Mutagenesis. Site-directed mutagenesis were performed on the rat nNOSoxy domain (amino acids 1−720), full-length rat nNOS (amino acids 1−1570), and mouse Δ65iNOS (amino acids 65−1269) using the mutagenesis kit from Stratagene. Mutation bases (bold and underlined) and a silent restriction site (*italic*) were introduced into the primers: W678A, 5′ ACT GGG TG**G CG**A TTG TGC CTC CCA TGT CG*G GAT CCA* TCA CCC CTG TCT TCC 3′; W678AR, 5′ GGA AGA CAG GGG TGA TG*G ATC CCG* ACA TGG GAG GCA CAA TC**G CC**A CCC AGT 3′; W678F, 5′ ACT GGG TGT **TC**A TTG TGC CTC CCA TGT CG*G GAT CCA* TCA CCC CTG TCT TCC 3′; W678FR, 5′ GGA AGA CAG GGG TGA TG*G ATC CCG* ACA TGG GAG GCA CAA TG**A AC**A CCC AGT 3′; W457A, 5′ GAA TGA GTA CCG GGC *C*CG *T*GG AGG CTG CCC GGC AGA CTG GATT**GC** GCT GGT CCC TCC AG 3′; and W457AR, 5′ CTG GAG GGA CCA GC**G C**AA TCC AGT CTG CCG GGC AGC CTC *CACGGG* CCC GGT ACT CAT TC 3′.

DNA isolation, restriction enzyme digestion, and transformation were carried out using standard protocols (*32*).

Protein Expression and Purification. Wild-type NOS enzymes and mutants contained a six-histidine tag and were overexpressed in *Escherichia coli* BL21 using the pCWori vector and purified as reported previously (*20*, *28*, *33*). NOS concentrations were determined from the 444 nm absorbance of the ferrous−CO complex, using an extinction coefficient of 76 mM^{-1} cm^{-1} (*34*).

Imidazole and Arg Binding Affinities. The binding affinity of Arg was measured by perturbation difference spectroscopy based on methods reported previously (*28*, *35*). In general, enzymes were incubated with H_4B overnight at 4 °C, and then known amounts of imidazole were gradually added to the diluted protein solution in cuvettes at 15 °C. Spectra were taken when equilibrium was reached after each addition. Plots of the peak to trough absorbance difference versus the imidazole concentration were fitted to give the apparent binding constant of imidazole. Attempts to determine the binding affinity of Arg were carried out in a similar way by gradually adding Arg to the H_4B- and imidazole-bound proteins.

Measurement of Apparent K_m Values for Arg or H_4B. Apparent K_m and V_{max} values were determined by fitting plots of the NO synthesis activity versus Arg or H_4B concentration. Each protein sample was incubated with Arg and H_4B for 30 min at room temperature before the assay. In the case of K_m measurements for Arg, mutant enzymes that were purified in the presence of Arg and H_4B were rapidly passed through a PD-10 desalting column to remove Arg from the enzyme and then immediately incubated with 200 μM H_4B and the indicated concentrations of Arg in the assay cuvette prior to initiation of the NO synthesis assay.

Dimerization Assessment. Protein stock solutions were incubated overnight at 4 °C in the presence of 1 mM H_4B and 10 mM Arg. The dimer:monomer content of the proteins was estimated by chromatography on an Amersham Pharmacia Biotech Superdex-200 HR size-exclusion column

equilibrated with 40 mM EPPS buffer (pH 7.6), containing 10% glycerol, 250 mM NaCl, and 3 mM DTT. The dimer:monomer content was derived from measuring the integrated area of the corresponding elution peaks determined at 280 nm. Molecular weights of the protein peaks were estimated relative to protein molecular weight standards (*35*, *36*).

NO Synthesis and NADPH Oxidation Rates. Steady-state rates of NO synthesis were determined by the spectrophotometric oxyhemoglobin assay using a difference extinction coefficient of 38 mM^{-1} cm^{-1} for the oxyhemoglobin to methemoglobin transition at 401 nm (*37*). Sample solutions contained 200 μM H_4B, 10 mM Arg, 0.6 mM DTT, 0.1 mg/mL BSA, 10 units/mL SOD, 346 units/mL catalase, 10 μM oxyhemoglobin, 4 μM FMN and FAD, and 0.1 μM NOS. For nNOS, 0.60 mM EDTA, 0.83 mM $CaCl_2$, and 12.5 μg/mL CaM were also added in the solution. Reactions were initiated by adding NADPH (final concentration of 100 μM), and the absorbance change at 401 nm was recorded at room temperature or 10 °C. For the NADPH oxidation rate measurements, we omitted oxyhemoglobin and used an extinction coefficient of 6.22 mM^{-1} cm^{-1} at 340 nm. In some cases, Arg was also omitted as explained in the text.

Formation of the Heme−Nitrosyl Complex during NO Synthesis. Aerated solutions containing 400 μM H_4B, 5 mM Arg, 1.2 mM DTT, 43 units/mL SOD, 3.5 units/μL catalase, and ~0.5−2 μM iNOS enzymes were rapidly mixed with an aerated solution of 130 μM NADPH at 10 °C in a stopped-flow spectrophotometer (Hi-Tech Ltd.). Spectral changes were recorded using a diode array instrument (Hi-Tech Ltd.). The absorbance change at 436 nm was used to follow formation of the heme−NO complex, and the absorbance change at 340 nm was used to follow NADPH oxidation in the reactions (*37*, *38*). The concentration of the ferrous heme−NO complex formed during the reactions was estimated from the absorbance change at 436 nm using an extinction coefficient of 48 200 M^{-1} cm^{-1} (*31*). At least 10 individual mixing experiments were averaged for each experiment to improve the signal-to-noise ratio. For experiments using nNOS and its mutants, 0.25 mM EDTA, 20 μM CaM, and 150 μM NADPH were also present in the solutions that contained 3.5−5 μM nNOS prior to mixing. The nNOS reactions were initiated by rapidly mixing the enzyme solution with an aerated buffer solution containing 2.83 mM $CaCl_2$.

Rates of Heme and Flavin Reduction. The kinetics of ferric heme reduction and flavin reduction were determined as described previously (*39*). Reactions were carried out at 10 °C in a stopped-flow spectrophotometer and were initiated by rapidly mixing an anaerobic buffered solution containing NOS enzyme, Arg, and H_4B with an anaerobic solution containing excess NADPH and a saturating concentration of CO. For nNOS, the reaction mixtures also contained CaM, Ca^{2+}, and EDTA at the concentrations indicated above. Heme reduction was followed by the absorbance increase at 444 nm due to formation of the ferrous−CO complex, while flavin reduction was followed from the absorbance decrease at 485 nm under the same conditions.

Kinetics of Ferrous Heme−NO Complex Formation and Oxidation. For the formation measurements, wild-type nNOSoxy and mutant proteins were diluted in 40 mM EPPS buffer (pH 7.6) that contained 40 mM Arg and 400 μM H_4B, were made anaerobic, and were then reduced with dithionite in an anaerobic optical cell (*18*, *40*). The ferrous protein solutions were transferred to the stopped-flow instrument using a gastight syringe and were then rapidly mixed at 10 °C with an anaerobic buffered solution containing 10 μM NO. Sequential spectral scans were collected and fit to an A → B reaction model using a Specfit global analysis program (Hi-Tech Ltd.). Eight to 10 scans were analyzed and then averaged for each experimental condition.

For the oxidation measurements, the procedure for forming ferrous nNOSoxy enzymes was identical to that described above. The ferrous proteins were then titrated by adding small amounts of an anaerobic NO-saturated buffer to form the ferrous NO complex, which was then transferred to the stopped-flow instrument and rapidly mixed at 10 °C with air-saturated buffer (*41*). Sequential spectral scans were collected and fit to an A → B reaction model using the Specfit global analysis program. Eight to 10 scans were analyzed and then averaged for each experimental condition.

Arg Hydroxylation Single-Turnover Reactions. Single-turnover reactions to study Arg hydroxylation by the nNOSoxy enzymes were carried out in the stopped-flow spectrophotometer at 10 °C as reported previously (*30*), in this case using nNOSoxy enzymes in the presence of 40 mM Arg and 400 μM H_4B.

Kinetics of H_4B Radical Formation During Arg Hydroxylation. Single-turnover Arg hydroxylation reactions were carried out as described previously (*30*). Briefly, an anaerobic buffer solution containing substrate, H_4B, and ~400 μM ferrous W678F nNOSoxy protein was rapidly mixed at 10 °C with equal amount of O_2-saturated buffer in a Hi-Tech rapid-quench instrument that was modified for rapid-freezing sample collection. The mixture was aged for various times, and then ejected into a rapid freezing solution housed in a bath apparatus from Update Instruments, Inc. (Madison, WI). The samples were then kept in liquid nitrogen until measurement. The EPR spectra of the frozen samples were recorded in a Bruker ER300 spectrometer equipped with an ER 035 NMR gauss meter and a Hewlett-Packard 5352B microwave power controller. Temperature control was achieved using Oxford Instruments ESR 900 continuous-flow liquid helium cryostat and ITC4 temperature controller. All spectra were recorded at 150 K using a microwave power of 2 mW, a frequency of 9.5 GHz, a modulation amplitude of 10 G, and a modulation frequency of 100 kHz.

Midpoint Potential Measurement of W457A iNOSoxy. The heme midpoint potential measurement was performed as previously described with some modifications (*42*). Spectroelectrochemical titrations were carried out at room temperature in the presence of 40 μM neutral red, 20 μM phenosafranin, and 100 μM methyl viologen. The W457A iNOSoxy (10 μM) was dissolved in a 40 mM phosphate buffer (pH 7.0) that included 200 μM H_4B and 4 mM Arg. Protein solutions and the working electrode (Au) were made anaerobic by alternating cycles of evacuation and flushing with nitrogen. The anerobic reference electrode [AgCl(s)/Ag(s)/Cl(aq)] and auxiliary electrode [Ag(s)/KCl(aq)] were promptly put into the cell under N_2 pressure. Reductive titrations were performed by gradually adding small amounts of current to the system using a Radiometer PGP201 potentiostat/galvanostat. Spectra were then recorded when the potential in the system stabilized after each addition. The midpoint potential was determined using the absorbance

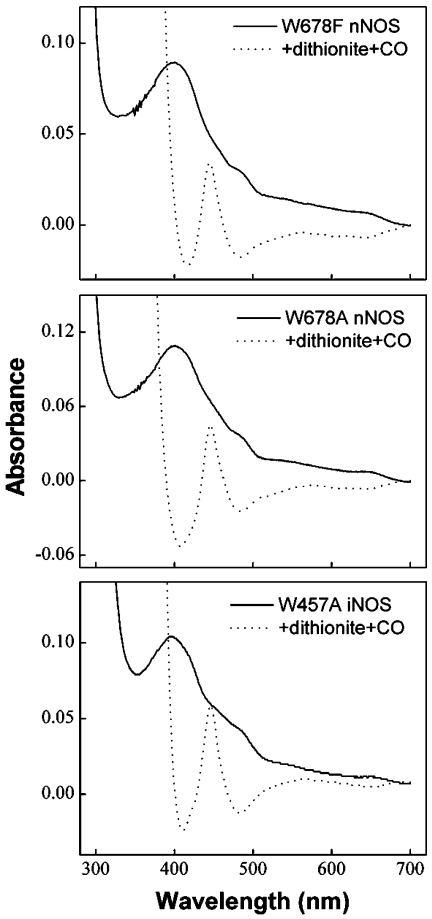

FIGURE 2: Spectral properties of the Trp mutants. Each panel shows the ferric enzyme in the presence of 200 μM H_4B and 5 mM Arg, and a difference spectrum created by subtracting the spectrum of the ferric enzyme from the spectrum of the enzyme ferrous−CO complex.

changes at 400 and 645 nm, which indicate the ferric to ferrous heme transition. At these wavelengths, changes due to the dye mediators are negligible. The midpoint potential was calculated according to the Nernst equation and is reported relative to the standard hydrogen electrode.

RESULTS

Spectral Properties, Stability, and Dimer Content of Mutants. The W678A and W678F nNOS proteins and W457A iNOS displayed Soret absorbance peaks at 418 nm when purified in the absence of H_4B and Arg, indicating that they contained low-spin heme iron as found in wild-type nNOS and W457A iNOSoxy when they are purified under similar conditions (*28*, *35*, *43*). When our mutants were purified in the presence of H_4B and Arg, they displayed Soret peak maxima at 398−400 nm, indicating that Arg and H_4B could bind and stabilize the heme iron in a five-coordinate high-spin state as in wild-type NOS (Figure 2). Addition of dithionite and CO to the mutants generated ferrous−CO complexes that had maximal Soret absorbance at 444 nm (Figure 2), similar to that of the wild type. These spectral properties demonstrate that the mutations do not significantly perturb the electronic properties of the heme or the spectral response to Arg and H_4B binding in nNOS or iNOS. This finding agrees well with crystal structures of iNOSoxy mutants W457A and W457F that show there are very limited structural changes compared to wild-type iNOSoxy (*27*).

The Trp678 nNOS mutants purified without Arg and H_4B were less stable in solution than the wild type and often precipitated during incubation at 15 °C. Adding NaCl increased their solution stabilities somewhat. These proteins also had difficulty binding Arg or H_4B, because incubating the mutants with either Arg or H_4B at 4 °C overnight did not cause a high-spin shift in the heme iron spin state that is characteristic of their binding (data not shown). However, we did observe the spin-state shift if the enzymes were incubated with H_4B and Arg, consistent with cooperative binding of these two molecules by NOS (*3*, *35*). However, even under this condition, their binding was slow, as judged by the spin-state shift, taking 1 h to be completed at 15 °C and ~25 min to be completed at room temperature when the mutants were incubated with 100 μM H_4B and 10 mM Arg (data not shown).

The dimer:monomer ratio of each Trp678 mutant was estimated by gel filtration chromatography (*28*, *35*). W678A nNOSoxy and W678F nNOSoxy that were purified in the absence of H_4B and Arg were approximately 45 and 55% dimeric, respectively, and preincubating either protein with Arg and H_4B alone or together increased their percentage of dimer by only 10%. In contrast, full-length nNOS Trp678 mutants that were purified with H_4B and Arg were approximately 95% dimeric (data not shown). Because of these properties, we henceforth utilized full-length and NOSoxy proteins that were purified in the presence of Arg and H_4B for our studies, unless noted otherwise.

Binding Affinity and Apparent K_m Values for H_4B and Arg. We attempted to determine K_s values for Arg by a method that relies on spectral change associated with Arg displacing imidazole that is bound to the NOS ferric heme (*28*, *44*, *45*). The K_s values for imidazole binding to wild-type nNOS and the W678A and W678F mutants were 200 (*46*), 102, and 93 μM, respectively, indicating similar affinities for imidazole. Unfortunately, during the subsequent Arg titrations, we observed only a partial displacement of bound imidazole in the mutants (data not shown), and consequently could not derive the Arg K_s values by this method. A similar situation was previously observed for the W457A and W457F iNOSoxy mutants (*28*). This suggests that the Trp mutations reduce the capacity of Arg to displace heme-bound imidazole in both nNOS and iNOS enzymes.

We then ran NO synthesis assays for each mutant to determine their apparent K_m values for H_4B and Arg. Because the mutant enzymes were purified in the presence of Arg and H_4B, they were buffer exchanged and then preincubated with the indicated concentrations of H_4B and Arg before the assay was carried out. Figure 3 shows how the NO synthesis activity of W457A iNOS increased as a function of preincubation time with 200 μM H_4B and 10 mM Arg at room temperature. Maximal activity required a 25 min preincubation period, so we routinely preincubated our mutant enzyme samples for 30 min at each concentration of H_4B or Arg prior to assaying for the NO synthesis activity. In Figure 4, the right panels are graphs of NO synthesis activity versus H_4B concentration for each of the Trp678 nNOS and Trp457 iNOS mutants, which were used to derive apparent K_m values for H_4B (Table 1). The left panels of Figure 4 contain graphs of NO synthesis versus Arg concentration for the same mutants and were used to derive apparent K_m values for Arg (Table 1). The apparent K_m values of W457A iNOS for Arg

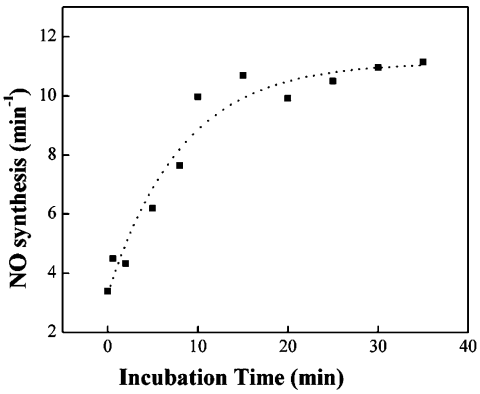

FIGURE 3: NO synthesis activity of W457A iNOS as a function of incubation time with H_4B. Sample solutions contained 10 mM Arg, 200 μM H_4B, 0.6 mM DTT, 0.1 mg/mL BSA, 10 units/mL SOD, 346 units/mL catalase, 10 μM oxyhemoglobin, 4 μM FMN and FAD, and 0.1 μM NOS. After incubation at room temperature for the indicated times, the reactions were initiated by adding 100 μM NADPH and the rate of absorbance change at 401 nm was recorded. Data are from two independent experiments.

or H_4B are both ~60−100 times greater than in wild-type iNOS. In contrast, the apparent K_m values for Arg in the W678F and W678A nNOS mutants are similar to that of wild-type nNOS, while their apparent K_m values for H_4B are 125 and 570 times greater than the wild-type value, respectively.

NO Synthesis and NADPH Oxidation. We next measured the rates of NO synthesis and NADPH oxidation at 25 and 10 °C. The measures were taken in the presence of H_4B and in the presence or absence of Arg. Enzymes were preincubated with H_4B and with or without Arg prior to the assay as required. Results are summarized in Table 2. Mutant NO synthesis activities determined at 25 or 10 °C were lower than in the wild-type enzymes. However, their concurrent rates of NADPH oxidation were either reduced to a lesser degree (W678A) or not reduced at all (W678F nNOS). Both the Ala and Phe mutants had decreased rates of NADPH consumption in the absence of Arg compared to the wild type.

NO synthesis from Arg displays a minimum stoichiometry of 1.5 NADPH molecules oxidized per NO molecule formed (*10*, *47*). This minimum value was observed for wild-type iNOS at 25 °C, while W457A iNOS had a value of 7. Similarly, we obtained values of 2, 8, and 16 for wild-type nNOS and its W678F and W678A mutants, respectively (Table 2). This indicates that a majority of the NADPH oxidation by the iNOS and nNOS Trp mutants is uncoupled from their NO synthesis.

Kinetics of Flavin and Heme Reduction. We measured rates of NADPH-dependent flavin and heme reduction at 10 °C in a stopped-flow spectrophotometer. Enzymes were mixed with excess NADPH under anaerobic conditions, and for heme reduction, the buffer included CO at a saturating concentration (*48*, *49*). The flavin reduction rates in the mutants were very similar to those of the wild-type enzymes (Table 3), consistent with the Trp mutations being located in the oxygenase domain and not affecting the flavoprotein domain. Figure 5 contains representative absorbance traces at 444 nm that indicate the ferric heme reduction rates in wild-type nNOS, iNOS, and the three mutants. The initial absorbance decrease that is present in some of the traces is due to flavin reduction that always takes place before electrons can transfer to the ferric heme (*31*, *37*). The heme reduction rates calculated from the data are listed in Table 3. Heme reduction was monophasic in nNOS, iNOS, and W678F nNOS. However, the rate in W678F nNOS was ~3 orders of magnitude slower than in wild-type nNOS. In contrast, heme reduction was biphasic in the W457A iNOS and W678A nNOS mutants, with the fast phase being a minor component of the total absorbance change in both cases (from 19 to 33%). The fast phase rate in W678A nNOS was 8 times slower than in the wild type, whereas in W457A iNOS, the fast phase was equivalent to that of the wild type. The slow phase in either Ala mutant was ~3 orders of magnitude slower than in the wild-type enzymes. To test if the slow rates of heme reduction were caused by a hindrance to CO binding, we measured rates of CO binding to the prereduced ferrous mutants. These rates were much faster than the aforementioned heme reduction rates (for example, the observed rate of CO binding by ferrous W457A iNOS was 25.2 s^{-1}), and thus indicated no hindrance toward CO binding in the mutants.

Heme Midpoint Potential. We determined the heme midpoint potential in W457A iNOSoxy to determine if the Trp mutation influences this thermodynamic parameter. A spectroelectrochemical reductive titration was performed for the ferric enzyme in the presence of Arg, H_4B, and mediator dyes (*42*, *50*). Representative data are shown in Figure 6. On this basis, the heme midpoint potential was estimated to be −271 ± 3 mV in W457A iNOSoxy, which is ~10−20 mV more negative than the heme midpoint values for wild-type iNOSoxy when measured under similar conditions [−263 mV (*50*)] (−253 mV).[2]

Steady-State Enzyme Distribution. Light absorbance spectra of the nNOS enzymes were recorded before and during NO synthesis to see if the Trp678 mutations might alter the amount of heme−NO complex that builds up during catalysis. The three panels in Figure 7 contain spectra recorded for each enzyme prior to NADPH addition (dotted line), after NADPH addition to reduce the enzyme flavins (dashed line), and after addition of Ca^{2+} to trigger CaM binding, ferric heme reduction, and NO synthesis (solid line). NADPH addition caused the flavins to become reduced as indicated by an absorbance decrease between 400 and 550 nm for each enzyme. During NO synthesis, there was a smaller buildup of six-coordinate ferrous heme−NO species in the W678A and W678F mutants compared to wild-type nNOS, as judged by their having smaller 437 nm peaks and a greater degree of ferric heme absorbance at 650 nm in the steady state. The amount of enzyme present as a six-coordinate heme−NO complex during NO synthesis was estimated using an extinction coefficient of 48 200 M^{-1} cm^{-1} at 437 nm (*31*) and found to be 60% for wild-type nNOS, 14% for W678A, and 25% for W678F. The mutant spectra also displayed a hump near 400 nm in the steady state, which could indicate buildup of other species such as a five-coordinate heme−NO complex, the heme−dioxy ($Fe^{II}O_2$) intermediate, or low-spin ferric heme.

Kinetics of Formation of the Heme−NO Complex and NADPH Oxidation during Catalysis. We next examined the

[2] J. Santolini and D. J. Stuehr, unpublished data.

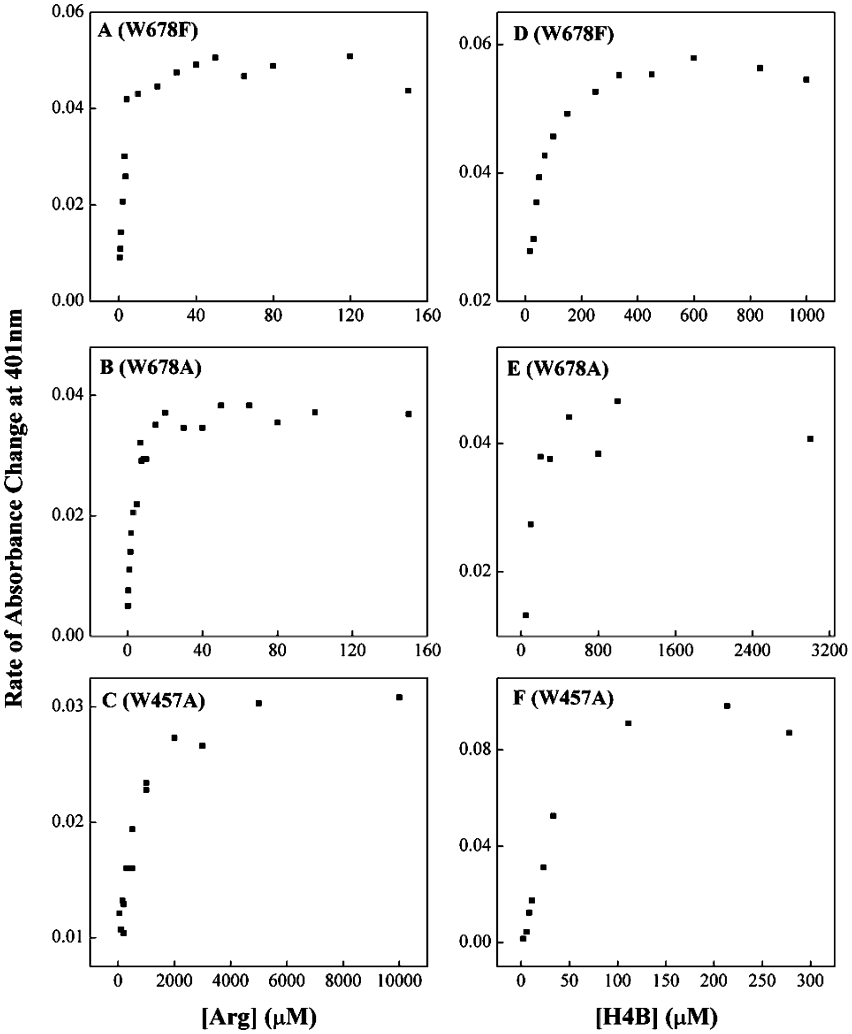

FIGURE 4: Apparent K_m determinations for Arg (left) and H_4B (right). Rates of NO synthesis were measured at room temperature using the oxyhemoglobin assay. Reaction mixtures contained the indicated concentrations of Arg (with a constant H_4B concentration of 200 μM) or the indicated concentrations of H_4B (with a constant Arg concentration of 10 mM). Enzymes were incubated in the assay mixture for 30 min prior to initiation of the reaction with NADPH. Data are representative of two similar experiments each.

Table 1: Apparent K_m Values for Arg and H_4B in Wild-Type and Mutant iNOS and nNOS[a]

	K_m(Arg) (μM)	K_m(H_4B) (μM)
iNOS fl	2.3[b]	1.6 ± 0.3[c]
W457A fl	273 ± 10	100 ± 29
nNOS fl	2.2[d]	0.2[e]
W678A fl	2.5 ± 0.1	114 ± 24
W678F fl	2.4 ± 0.2	25 ± 1

[a] Values were determined using the oxyhemoglobin NO synthesis activity assay as described in Experimental Procedures. Values are the mean and standard deviation that were derived from graphic analyses. [b] Data from ref *66*. [c] Data from ref *22*. [d] Data from ref *7*. [e] Data from ref *3*.

Table 2: NO Synthesis and NADPH Oxidation Activities in the Presence or Absence of Arg[a]

		H_4B + Arg		H_4B	
	enzyme	NO synthesis (min^{-1})	NADPH oxidation (min^{-1})	NO synthesis (min^{-1})	NADPH oxidation (min^{-1})
	WT iNOS	96 ± 5	140 ± 6	ND	ND
	W457A	5.9 ± 0.5	44 ± 7	ND	ND
25 °C	WT nNOS	72 ± 2	145 ± 7	0	161 ± 6
	W678A	6.5 ± 0.6	103 ± 1	0	107 ± 3
	W678F	20 ± 1	153 ± 7	0	142 ± 3
	WT nNOS	34 ± 2	76 ± 2	0	125 ± 6
10 °C	W678A	5.0 ± 0.6	77 ± 6	0	76 ± 2
	W678F	11.3 ± 0.9	82 ± 7	0	84 ± 2

[a] Assays were run at the two indicated temperatures. The turnover number is expressed as the moles of product formed per mole of heme per minute. Data are the mean and standard deviation of three determinations. WT is wild type and ND not determined.

kinetics of formation of the heme−NO complex and NADPH oxidation just after initiating NO synthesis in wild-type nNOS (*31*) and in the Trp678 mutants. The NADPH-reduced, anaerobic, CaM-free enzymes were rapidly mixed in the stopped-flow spectrophotometer with an aerated buffer containing Ca^{2+} to trigger CaM binding and initiate NO synthesis at 10 °C (*31*, *51*). Formation of the heme−NO complex was monitored by the absorbance gain at 436 nm, and concurrent NADPH oxidation was monitored by the absorbance loss at 340 nm. In Figure 8, the left panels depict light absorbance spectra that were collected just after mixing to initiate the reaction, during NO synthesis, and after NO synthesis had ceased (due to NADPH depletion) for wild-type nNOS and the two Trp678 mutants. The corresponding absorbance changes at 437 and 340 nm that took place during the reactions are shown in the middle and right panels of Figure 8. The spectral traces in the left panels confirm that

Table 3: Observed Rates of NADPH-Dependent Flavin and Heme Reduction[a]

	flavin reduction (s^{-1})		heme reduction (s^{-1})	
NOS	k_1 (%)	k_2 (%)	k_1 (%)	k_2 (%)
WT nNOS	14.5 ± 1.9 (60%)	3.3 ± 0.4 (40%)	4.8 ± 0.11 (100%)	
W678F	13.8 ± 5.5 (40%)	3.3 ± 0.7 (60%)	0.0068 ± 0.0003 (100%)	
W678A		ND	0.61 ± 0.02 (19%)	$(62 \pm 2.9) \times 10^{-5}$ (81%)
WT iNOS	5.2 ± 0.7 (60%)	0.76 ± 0.19 (40%)	0.61 ± 0.01 (100%)	
W457A	7.24 ± 1.0 (63%)	1.2 ± 0.5 (37%)	0.71 ± 0.08 (33%)	0.026 ± 0.006 (67%)

[a] Reactions were initiated in a stopped-flow instrument at 10 °C. Data are the mean and standard deviation and are representative of two separate experiments for each enzyme. WT is wild type and ND not determined.

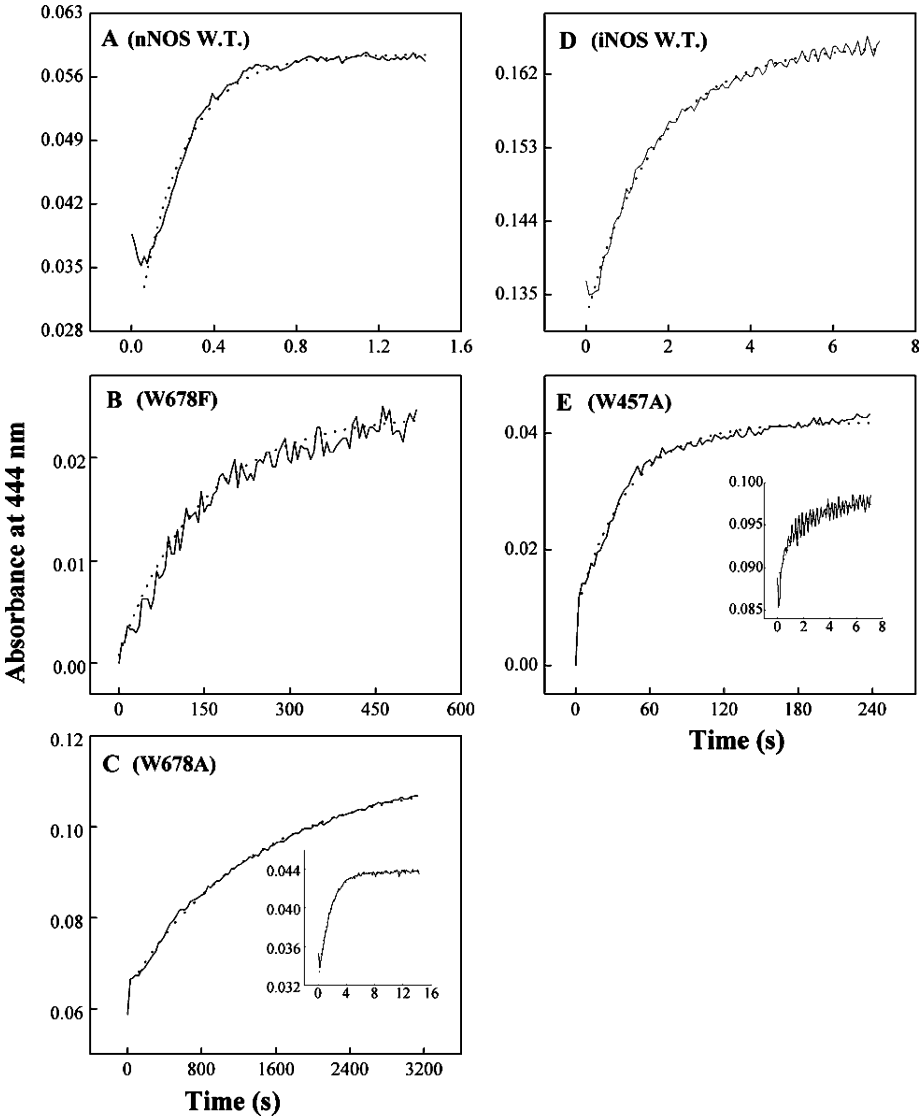

FIGURE 5: Kinetics of ferric heme reduction. Anaerobic ferric enzyme solutions containing 400 μM H_4B, 10 mM Arg, 1.2 mM DTT, 2 μM CaM (for nNOS proteins), 1.2 mM $CaCl_2$ (for nNOS proteins), and ~0.8−2 μM NOS were rapidly mixed at 10 °C with an anaerobic CO-saturated buffer solution containing 100 μM NADPH. Heme reduction was followed by formation of the ferrous−CO complex at 444 nm. Dotted lines are the fitting curves. Inset plots in panels C and E show the absorbance changes over shorter time frames.

there was less buildup of a six-coordinate heme−NO complex during NO synthesis in the Trp678 mutants than in wild-type nNOS. The absorbance increases at 437 nm were best fit to a two-exponential equation for all three enzymes, as reported previously for wild-type nNOS (*31*, *51*). However, the fast and slow phases were 4−10 times slower in the Trp678 mutants than in wild-type nNOS (Table 4). In wild-type nNOS, the heme−NO complex buildup was associated with a 10-fold deflection in the rate of NADPH oxidation (rates listed in Table 4), similar to what was reported previously (*31*, *51*). After ~2 s, the wild-type enzyme reaction reached a steady-state phase where the concentration of the heme−NO complex and the NADPH oxidation rate remained relatively constant until the NADPH became depleted (middle panels, Figure 8). After this point, the absorbance at 437 nm decreased to a level that was 0.02 absorbance unit above the original value, which takes into account an absorbance increase that occurs at this wavelength due to reoxidation of the nNOS flavins (see spectral traces in the left panel). In contrast, for the Trp678 mutants, the

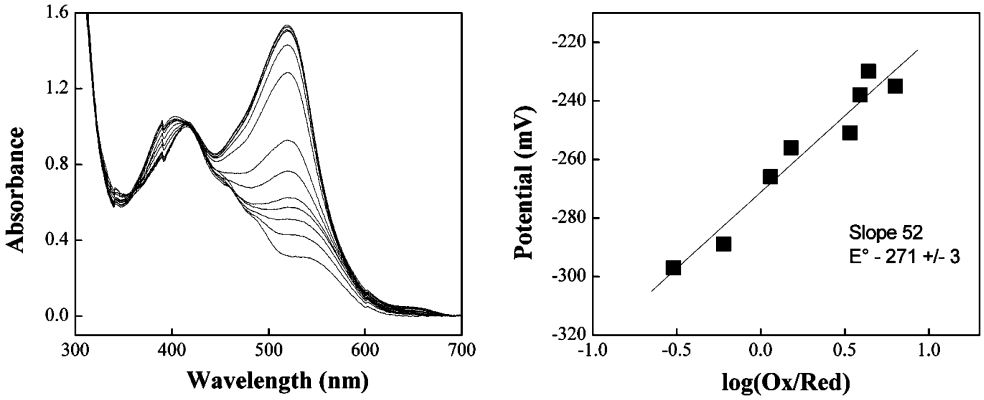

FIGURE 6: Potentiometric reductive titration of W457A iNOSoxy. The left panel shows spectra recorded during titration of the ferric enzyme in the presence of H_4B, Arg, and mediator dyes. The right panel plots the measured potentials vs the logarithmic ratio of ferric: ferrous heme.

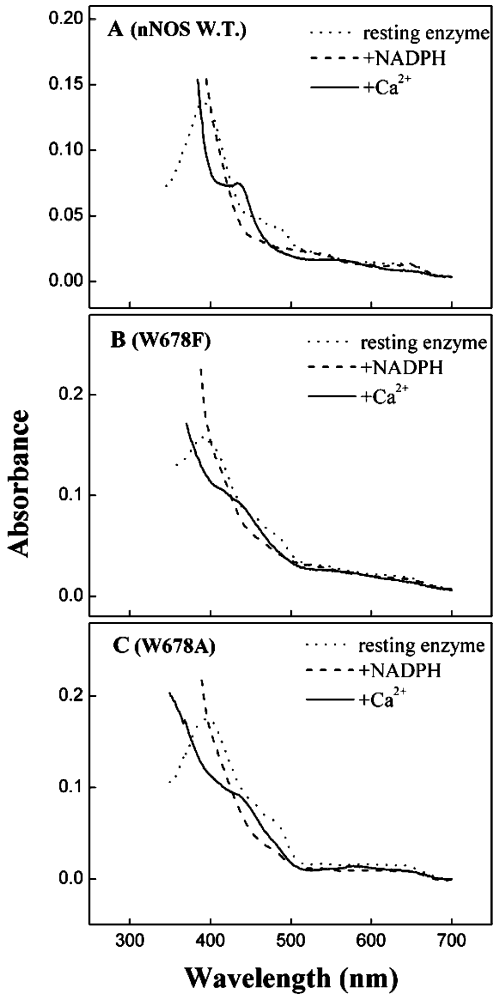

FIGURE 7: Light absorbance spectra for nNOS proteins recorded before and during NO synthesis. Reaction mixtures contained 200 μM H_4B, 5 mM Arg, 0.6 mM DTT, 2 μM CaM, 0.25 mM EDTA, and ~2 μM NOS. Dotted lines are the spectra of the initial CaM-free, ferric enzymes. Dashed lines are the spectra recorded after adding 100 μM NADPH to each enzyme solution. Solid lines are the spectra recorded after initiating NO synthesis by adding 1.2 mM Ca^{2+}. Data are representative of three identical trials.

absorbance gain at 437 nm indicating buildup of the heme−NO complex was more gradual and much smaller and did not reach a clear steady state prior to NADPH depletion. Again, the 437 nm absorbance signals did not return to their initial values after the NADPH was consumed in either mutant reaction (middle panels, Figure 8) because of their being offset by an absorbance gain due to the reoxidation of the flavins (see spectral traces in the left panels). There was an initial rapid NADPH oxidation in the W678F and W678A mutant reactions that consumed 1.5 and 1.3 NADPH molecules per mole of enzyme, respectively, and took place prior to significant buildup of the heme−NO complex. These initial rates of NADPH consumption were either equivalent to (W678F) or slightly slower than (W678A) the initial rate seen in the wild-type nNOS reaction (see NADPH oxidation k_1 values in Table 4). The subsequent buildup of the heme−NO complex in either Trp678 mutant was not associated with a clear deflection of their NADPH consumption rates, consistent with only a small proportion of each mutant enzyme accumulating as a heme−NO complex. The NADPH oxidation rates during NO synthesis were then calculated from the slopes of the absorbance decrease at 340 nm within the 2−8 s time window (Figure 8). This showed that the mutant NADPH oxidation rates were either equivalent to (W678A) or greater than (W678F) the rate of NADPH oxidation by wild-type nNOS (see NADPH oxidation k_2 values in Table 4). This relationship corresponds with what we observed for the mutant NADPH oxidation rates when they were measured during NO synthesis in a conventional spectrophotometer at 10 °C (Table 2). The stopped-flow data suggest that the Trp678 mutants catalyze uncoupled NADPH oxidation even in the initial very early phase of their NO synthesis.

Heme−NO Binding Kinetics and Oxidation Rate of the Ferrous Heme−NO Complex. Because NO binding kinetics and stability of the heme−NO complex are altered in some NOS mutants (*39*, *40*), we examined these properties in W678A and W678F nNOSoxy. The formation rates and stabilities of their ferrous heme−NO complexes were determined in stopped-flow reactions that mixed dithionite-reduced nNOSoxy mutants in the presence of H_4B and Arg with a 10 μM NO solution under anaerobic conditions. The light absorbance data shown in Figure 9 (left panels) indicate that both mutants predominantly formed stable six-coordinate ferrous heme−NO complexes whose spectral features were similar to those of the wild-type ferrous heme−NO complex, with the exception that the Soret peak of either mutant was broader on its left (lower wavelength) side. The right panels in Figure 9 depict the kinetics of ferrous enzyme disappearance and heme−NO complex formation during the NO

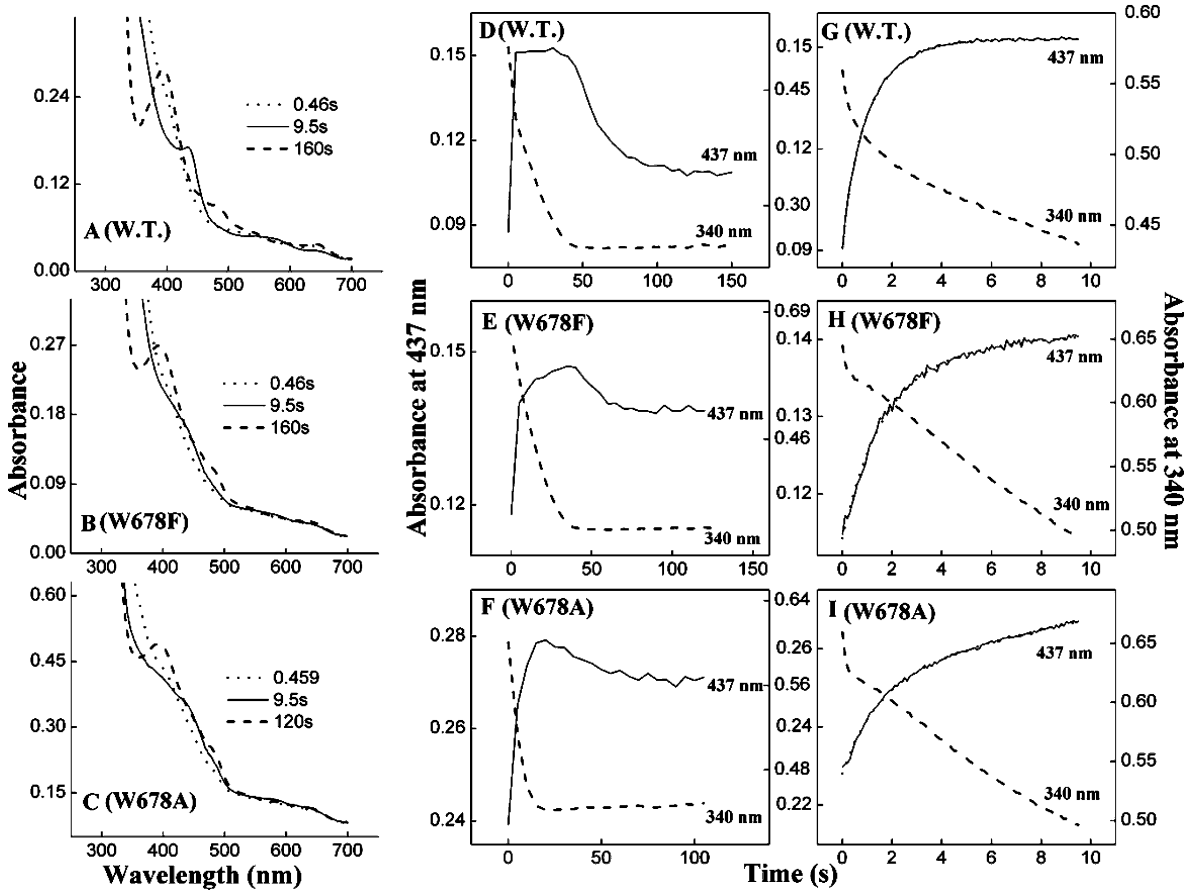

FIGURE 8: Kinetics of the buildup and decay of the heme−NO complex and simultaneous NADPH oxidation during NO synthesis. Aerated solutions containing 400 μM H_4B, 5 mM Arg, 1.2 mM DTT, 20 μM CaM, 0.25 mM EDTA, 3.5−5 μM NOS enzyme, and 150 μM NADPH were rapidly mixed at 10 °C with aerated solutions of 2.83 mM $CaCl_2$ in a stopped-flow spectrophotometer. The left panels depict absorbance traces collected at the indicated times after mixing. Middle and right panels depict the kinetics of absorbance change at 436 nm for following formation of the heme−NO complex (solid lines) and the kinetics of absorbance change at 340 nm for following NADPH oxidation (dashed lines). The kinetic traces in the middle and right panels were generated by subtracting the absorbance values at 700 nm from concurrent absorbance values at 436 nm (or 340 nm). Fits to the 437 nm absorbance traces are shown as dotted lines in panels G−I. Data are representative of two or three separate experiments for each enzyme.

Table 4: Observed Rate Constants for Formation of the Heme−NO Complex and NADPH Consumption after Initiation of NO Synthesis[a]

	heme−NO complex formation rate (s^{-1})		NADPH consumption rate (s^{-1})		
NOS	k_1 (%)	k_2 (%)	k_1	k_2	% NO complex
WT nNOS	3.3 ± 0.4 (18%)	0.83 ± 0.01 (82%)	0.021	0.0019	60
W678F	0.64 ± 0.01 (79%)	0.16 ± 0.01 (21%)	0.021	0.0038	25
W678A	0.77 ± 0.07 (39%)	0.08 ± 0.03 (61%)	0.017	0.0022	14

[a] NO synthesis was initiated in a stopped-flow spectrophotometer at 10 °C. The percentages in parentheses give the proportion of absorbance change for each kinetic phase. The k_1 and k_2 for NADPH consumption are the approximate linear rates observed between 0 and 0.4 s and between 2 and 8 s after mixing, respectively. Data are representative of two or three similar experiments. WT is wild type.

binding reaction. The transitions were monophasic, and the observed rates of formation of the ferrous heme-NO complex were 62 ± 11, 59 ± 9, and 27 ± 4 for W678F, W678A, and wild-type nNOSoxy, respectively, under our experimental conditions, indicating that the Trp678 mutations do not greatly alter the kinetics of binding of NO to the heme.

The oxidation rate of the NOS ferrous heme−NO complex is a key parameter that helps determine NO synthesis activity (*52*). This parameter (k_{ox}) exhibits a 10-fold range among the three mammalian NOSs (*39*, *41*). We determined k_{ox} values for the wild-type and mutant nNOSoxy proteins by mixing their ferrous heme−NO complexes with air-saturated buffer in stopped-flow reactions and following their subsequent conversion to the ferric enzyme (*39*, *41*). In Figure 10, the left panels depict the light absorbance spectra of the beginning ferrous heme-NO species and ending ferric heme species in each reaction, while the right panels depict the time courses of their disappearance and appearance, respectively. The transitions were monophasic, and the derived k_{ox} values were 0.20 ± 0.01, 0.30 ± 0.01, and 0.30 ± 0.1 s^{-1} for wild-type, W678A, and W678F nNOSoxy, respectively. This indicates that the Trp678 mutants have k_{ox} values that are similar to that of wild-type nNOSoxy.

Kinetics of Heme H_4B Transitions during Arg Hydroxylation. To determine if the Trp678 mutations altered the kinetics of Arg hydroxylation, we monitored the heme transitions that occur during a single-turnover Arg hydroxylation reaction carried out at 10 °C in the stopped-flow spectrophotometer. Air-saturated buffer was mixed with anaerobic ferrous nNOSoxy proteins that contained H_4B and

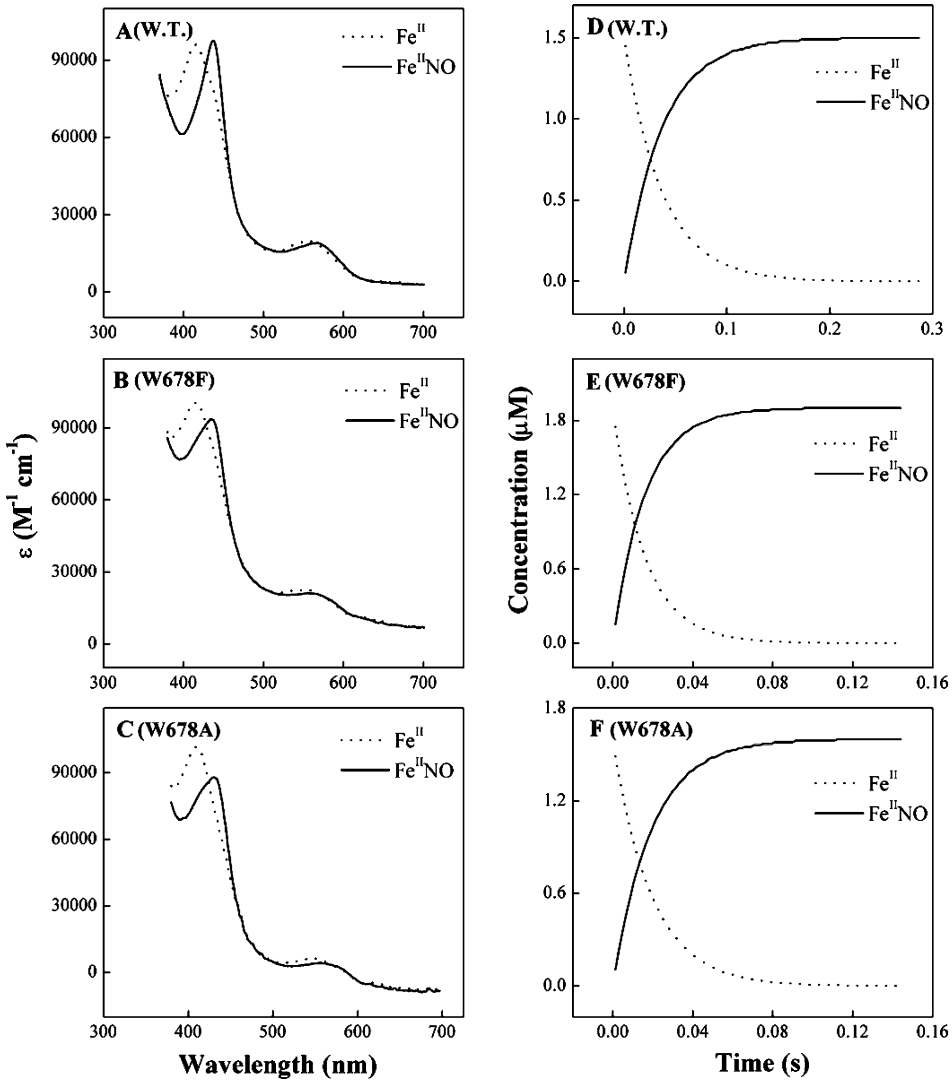

FIGURE 9: Binding of NO to the ferrous nNOSoxy proteins. Anaerobic ferrous nNOSoxy proteins in the presence of Arg (40 mM) and H_4B (400 μM) were rapidly mixed in a stopped-flow instrument with a 10 μM anaerobic NO solution at 10 °C. The left panels depict spectra of the beginning ferrous and ending $Fe^{II}NO$ species as calculated from global analysis of the kinetic data. The right panels show the concentration of both species vs time after mixing. Data are representative of two similar experiments.

Arg, and the subsequent heme transitions were followed by UV−visible scanning (*18*, *30*, *53*). Figure 11 depicts representative data collected during reactions catalyzed by wild-type, W678A, and W678F nNOSoxy. The left panels show the light absorbance spectra of the three enzyme species that were detected during each reaction, while the right panels show how the concentration of each species changed with time during the reaction. In all three cases, we could identify a beginning ferrous species, a heme−dioxy ($Fe^{II}O_2$) intermediate, and an ending ferric species. Their calculated Soret absorbance maxima are listed in Table 5. Formation and disappearance of the $Fe^{II}O_2$ intermediate were best described by monophasic transitions, consistent with previous reports (*18*, *53*). The kinetics of $Fe^{II}O_2$ formation in the mutants were similar to or somewhat less than the rate in wild-type nNOSoxy (Table 5). However, the transition of the $Fe^{II}O_2$ intermediate to ferric enzyme was 2.8 and 5.6 times slower in the W678F and W678A nNOSoxy mutants, respectively, than in the wild type (Table 5). On the basis of our work with the analogous W457A and W457F iNOSoxy mutants (*30*), the kinetic differences we observed here regarding $Fe^{II}O_2$ disappearance rates in the Trp678 nNOSoxy mutant reactions imply that their rates of $Fe^{II}O_2$ reduction by H_4B are proportionally slower (*18*, *30*).

We tested this possibility by measuring the rate of H_4B radical formation during the Arg single-turnover reaction catalyzed by W678F nNOSoxy at 10 °C (data not shown). The rate of H_4B radical formation was 5 s^{-1}, similar to the rate of $Fe^{II}O_2$ disappearance in the same reaction (5.2 s^{-1}, Table 5). This supports the contention that $Fe^{II}O_2$ reduction by H_4B is slower in the Trp678 nNOS mutants.

DISCUSSION

Here we investigated how mutations of a conserved Trp known to influence H_4B electron transfer (*24*, *30*) would impact NADPH-driven NO synthesis by nNOS and iNOS. As expected, mutation of this Trp affected many enzyme properties, consistent with its indole engaging in an extensive π-stacking interaction with H_4B (*27*) and with H_4B modulating the structural, electronic, binding, thermodynamic, and kinetic properties of NOS (*54*, *55*). Fortunately, the negative effects caused by the mutations on NOS protein solubility, dimer stability, and Arg or H_4B binding affinity were largely overcome by purifying, preincubating, and assaying the

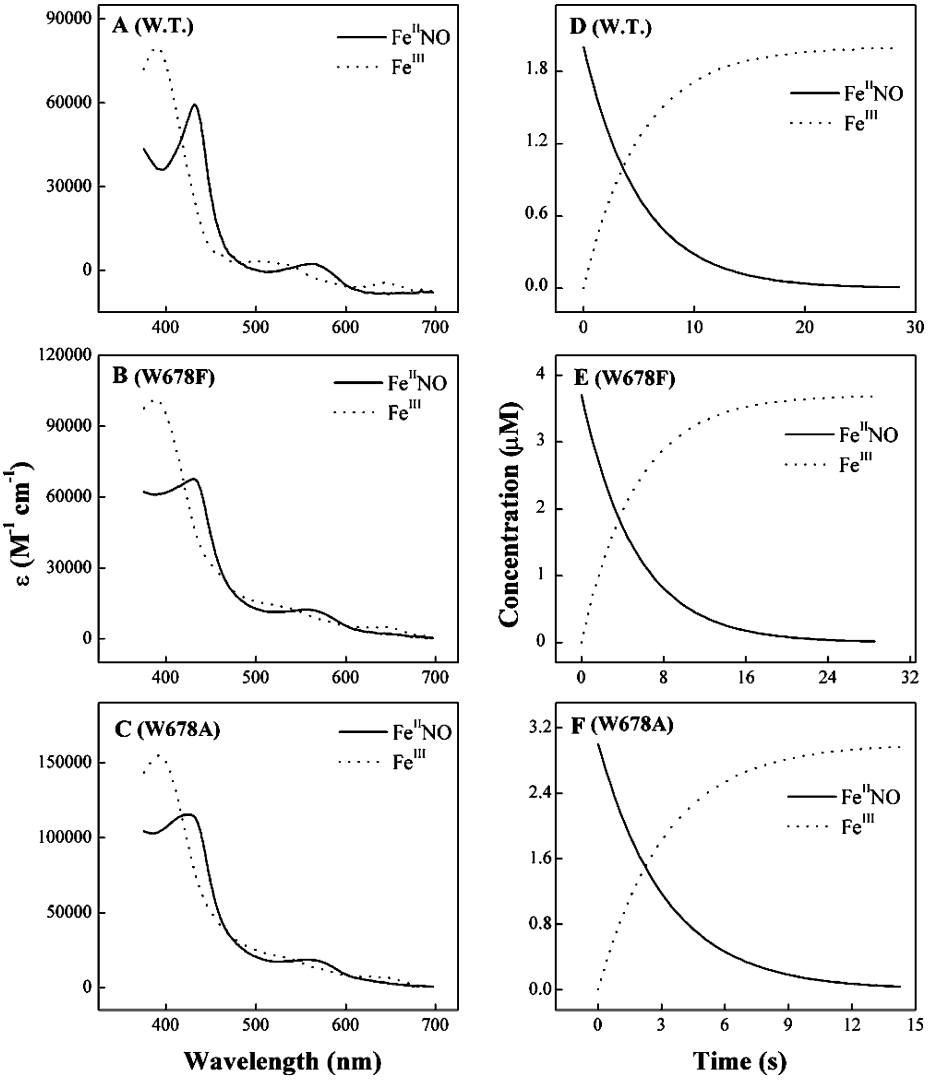

FIGURE 10: Spectra and kinetics of nNOSoxy $Fe^{II}NO$ oxidation reactions. Anaerobic ferrous nNOSoxy proteins in the presence of Arg (40 mM) and H_4B (400 μM) were titrated with small amounts of anaerobic NO-saturated buffer to form the ferrous NO complex, which was then rapidly mixed in a stopped-flow spectrophotometer with air-saturated buffer at 10 °C. Panels A−C depict spectra of the beginning ferrous−NO and ending ferric heme species as calculated by global analysis of the spectral data, while panels D−F show the concentrations of both species vs time after mixing. Data are representative of three experiments.

mutants in the presence of sufficiently high concentrations of Arg and H_4B. However, even under this circumstance, the Trp mutants displayed lower NO synthesis activities and uncoupled NADPH oxidation. Our additional measures identified the mechanisms responsible for the catalytic phenotype, as discussed below.

In general, the lower NO synthesis activities of the Trp mutants could arise for two different reasons. (A) Mutant enzyme molecules generate NO more slowly than the wild type, or (B) a smaller subset of the mutant enzyme molecules generate NO at the normal rate. Our data suggest that both circumstances are at play for the Trp mutants, causing them to have a slower and less efficient NO synthesis. Consider the spectral data we collected during NO synthesis by the Trp678 nNOS mutants, which showed that the heme−NO complex builds up more slowly and to a smaller extent than in wild-type nNOS. The speed and extent of the buildup of the heme−NO complex depends on the intrinsic rate of NO biosynthesis (which is limited by k_r, the rate of ferric heme reduction by the NOS flavoprotein domain), the kinetics of heme−NO association and dissociation, the stability of the six-coordinate heme−NO complex, the rate of reaction between the ferrous heme−NO complex and O_2 (specified by kinetic parameter k_{ox}), and, finally, the proportion of total NOS molecules that generate NO in unit time (*41*). Our related measures can dismiss some of these potential contributors. For example, the Trp678 NOSoxy mutants formed stable six-coordinate ferrous and ferric heme−NO complexes, had relatively normal NO binding kinetics, and had k_{ox} values similar to those of wild type nNOS. Thus, their diminished heme−NO complex formation during steady-state NO synthesis was potentially due to their having a slower rate of NO biosynthesis and/or fewer enzyme molecules making NO in unit time.

The rates of ferric heme reduction in the Trp678 nNOS mutants were up to 1000 times slower than in wild-type nNOS when they were measured at 10 °C under a CO atmosphere. Unfortunately, these rates are much too slow to account for the rates of buildup of the heme−NO complex and NO synthesis that we observed for these mutants in our aerobic experiments. Such "O_2 enhancement" of the ferric heme reduction rate has been observed before in eNOS (*56*) and in certain nNOS mutants (*48*), and its basis remains to be explained. However, in this study, the O_2 effect seen in

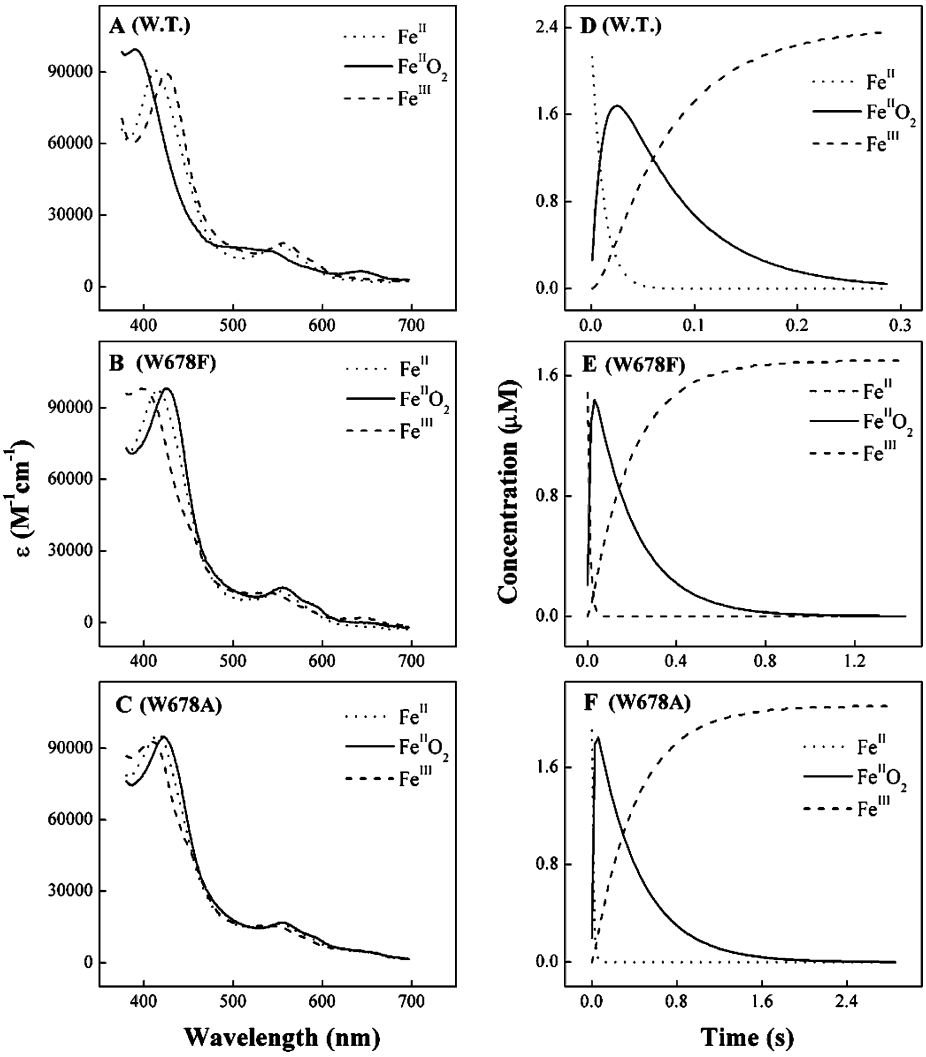

FIGURE 11: Heme transitions and kinetics during single-turnover Arg hydroxylation reactions catalyzed by nNOSoxy proteins. Anaerobic ferrous nNOSoxy proteins (4 μM) in the presence of Arg (40 mM) and H_4B (400 μM) were mixed in a stopped-flow instrument with air-saturated buffer at 10 °C, and diode array spectra were collected. Panels A−C show the three heme species that were detected during each reaction as calculated by global analysis of the spectral data, while panels D−F show their concentration profiles vs time after mixing. Data are representative of three similar experiments.

Table 5: Light Absorbance and Kinetic Data for the Heme Transitions during Single-Turnover Arg Hydroxylation Reactions[a]

protein	Soret absorbance peak positions (nm)			$Fe^{II}O_2$ formation rate (s^{-1})	$Fe^{II}O_2$ oxidation rate (s^{-1})
	Fe^{II}	$Fe^{II}O_2$	Fe^{III}		
WT nNOSoxy	413	426	390	81 ± 5.1	14.5 ± 0.31
W678F	415	426	397	102 ± 6.2	5.2 ± 0.22
W678A	414	423	408	56 ± 2.1	2.6 ± 0.17

[a] Anaerobic ferrous nNOSoxy proteins that contained Arg and H_4B were mixed with an aerated solution in a stopped-flow instrument to initiate Arg hydroxylation at 10 °C. Absorbance peaks and transition rates were calculated by global analysis. Data are representative of two separate experiments.

the Trp mutants could involve a change in the thermodynamic driving force for their ferric heme reduction, given that the heme midpoint potential was somewhat decreased in the W457A mutant compared to that of the wild type. In any case, we can obtain reasonable estimates for the rates of ferric heme reduction under aerobic conditions from the NADPH oxidation rates that were measured in the absence of Arg (*31*). These measures indicated that electron flux through the heme of the W678A and W678F nNOS mutants was diminished to 66 and 78% of that of wild-type nNOS, respectively. This suggests that the mutants do have somewhat slower rates of ferric heme reduction, consistent with their having decreased NO synthesis activity and smaller buildup of the heme−NO complex.

This leaves us to consider what proportion of the mutant enzyme molecules engage in NO synthesis in unit time. The degree to which product formation is coupled to ferric heme reduction in NOS enzymes can be determined in single-turnover Arg hydroxylation reactions catalyzed by ferrous NOSoxy domains (*18*, *30*, *53*, *57*, *58*). Our previous studies with W457A and W457F iNOSoxy mutants established that they have slower rates of H_4B electron transfer to the $Fe^{II}O_2$ intermediate, and this kinetic defect is associated with a proportionally slower disappearance of their $Fe^{II}O_2$ intermediate and with a proportionally slower and less efficient Arg hydroxylation (*30*). Specifically, the rate of disappearance of the $Fe^{II}O_2$ intermediate (which is determined by the rate of H_4B radical formation) was 12.5 s^{-1} in the wild-type iNOSoxy reaction, but fell by 50 and 75% in the W457F and W457A iNOSoxy reactions, respectively (*30*). These slower rates of H_4B electron transfer were associated with

60 and 73% less Arg hydroxylation per heme in the iNOSoxy single-turnover reactions. In this study, we observed slower rates of $Fe^{II}O_2$ disappearance in the Arg hydroxylation reactions catalyzed by the W678F and W678A nNOSoxy mutants, and slower H_4B radical formation in the W678F nNOSoxy reaction, quite similar to what was observed in the iNOSoxy counterparts. This strongly implies that the Trp678 mutants also exhibit slower $Fe^{II}O_2$ reduction by H_4B, and therefore catalyze a less coupled Arg hydroxylation.

If two mutational effects are in play in our W678F and W678A mutants (i.e., a slower ferric heme reduction by the flavoprotein domain and a slower $Fe^{II}O_2$ reduction by H_4B), can we discern their individual impacts on catalysis? To address this, we ran computer simulations of a global kinetic model for NOS catalysis, to examine how slowing the rate of ferric heme reduction, on its own, will impact buildup of the heme−NO complex and NO synthesis activity in nNOS. As previously explained in detail (*41*, *51*, *52*), the global kinetic model relies on the finding that under conditions of sufficient substrate concentrations the steady-state enzyme distribution and NO synthesis activity of a given NOS are largely determined by three kinetic parameters: the rate of ferric heme reduction (k_r), the rate of NO dissociation from the ferric heme−NO product complex (k_d), and the oxidation rate of the ferrous heme−NO complex (k_{ox}). The simulations run here[3] revealed that the k_r values of the W678F and W678A nNOS mutants would have had to drop to 35 and 23% of the value of wild-type nNOS, respectively, to fully account for their smaller degree of heme−NO complex buildup seen during their NO synthesis. However, such decreases in k_r are not supported by the NADPH oxidation rates that we measured for the mutants in the absence of Arg, which ranged from 61 to 78% of that of wild-type nNOS. In addition, experimental work in which the k_r of nNOS was decreased to different degrees through the use of CaM mutants (*51*, *59*) provides independent evidence that k_r would have to fall below 40% of the wild-type value to approach the diminished levels of NO synthesis activity and heme−NO complex buildup that we observed in our W678F and W678A nNOS mutants. Thus, the slower k_r values in the Trp678 nNOS mutants appear to account for only approximately one-third of the overall effect regarding their diminished heme−NO complex buildup and NO synthesis rates. This implies that an uncoupled NO biosynthesis, caused by slower H_4B electron transfer to the $Fe^{II}O_2$ intermediate, accounts for the remaining two-thirds of the overall effect. Our current analysis therefore supports the original proposal developed from experiments with NOSoxy enzymes (*17*, *30*) that slowing H_4B electron transfer would decrease the efficiency of NADPH-driven NO synthesis by full-length NOS enzymes.

It is interesting to consider how the H_4B electron transfer step and the ferric heme reduction step might be influenced by the Trp mutations. The mechanisms by which Trp457 influences the rate of H_4B electron transfer in iNOSoxy, and how this in turn impacts the efficiency of its product formation in single-turnover reactions, have been previously discussed in detail (*27*, *30*, *53*, *60*). Briefly, the structural and electronic changes brought on by the Phe and Ala substitutions appear to prevent NOS from maximally stabilizing its H_4B radical. This in turn slows the rate of H_4B radical formation and consequently the rate of $Fe^{II}O_2$ reduction by H_4B. A slower reduction of the $Fe^{II}O_2$ intermediate increases the probability that it will decay to superoxide and ferric enzyme before it can be reduced by H_4B (Scheme 1). Such a decay process for the $Fe^{II}O_2$ intermediate uncouples ferric heme reduction from Arg hydroxylation (*61*), and this helps to explain why the iNOS and nNOS Trp mutants studied here have such poor coupling regarding their NADPH-driven NO synthesis. Perhaps more surprising was that the Trp678 mutations have an effect on the rate of ferric heme reduction in nNOS. Ferric heme reduction is catalyzed exclusively by the FMN hydroquinone of the NOS flavoprotein domain, and this electron transfer step is subject to its own unique regulation (*16*, *48*, *51*, *59*, *62*, *63*). The FMN module must dock against the NOS oxygenase domain to transfer an electron to the heme; however, this process is thought to involve surface residues that are far from Trp678 (*12*, *16*, *29*), and the crystal structures of the W457A and W457F iNOSoxy mutants do not exhibit any obvious structural change in that surface region of iNOSoxy (*27*). Thus, we speculate that the Trp mutations might impact ferric heme reduction through an effect on the heme itself, either by lowering the heme midpoint potential, as seen here, or by altering some other aspect of the heme, such as the degree of heme ruffling that occurs in response to H_4B binding (*64*). In any case, during nNOS catalysis, the Trp678 mutations appear to slow ferric heme reduction by a factor of less than 2, so the physical basis for the effect might be relatively subtle.

Relation to Other Studies. Our W678F and W678A nNOS mutants have properties that are both similar to and different from those reported previously for nNOS mutants W678L and W678H (*29*). For example, our mutants form homodimers to a greater degree when provided with Arg and H_4B and have relatively normal K_m values for Arg, whereas the W678L mutant in particular exhibits very poor dimerization and Arg binding. Both pairs of mutants have a poorer affinity for H_4B relative to wild-type nNOS, and all have diminished levels of NO synthesis, uncoupled NADPH oxidation, and a kinetic defect in their ferric heme reduction when measured under anaerobic conditions. Sagami et al. (*29*) concluded that Trp678 is important to the retention of the appropriated active site conformation for H_4B and Arg binding and for electron transfer from NADPH to the heme. Our findings concur with theirs, but in addition emphasize that the ability of Trp678 to regulate H_4B electron transfer to the $Fe^{II}O_2$ intermediate is likely to be its most important effect with regard to its impact on the catalytic functioning of nNOS.

[3] In the simulations, we varied k_r, utilized our measured k_{ox} values, and assumed that the Trp mutants had identical k_d values as in wild-type nNOS (*65*).

REFERENCES

1. Stuehr, D. J., and Ghosh, S. (2000) in *Handbook of Experimental Pharmacology* (Mayer, B., Ed.) pp 33−70, Springer-Verlag, Berlin.
2. Alderton, W. K., Cooper, C. E., and Knowles, R. G. (2001) Nitric oxide synthases: Structure, function and inhibition, *Biochem. J. 357*, 593−615.
3. Gorren, A. C., List, B. M., Schrammel, A., Pitters, E., Hemmens, B., Werner, E. R., Schmidt, K., and Mayer, B. (1996) Tetrahydrobiopterin-free neuronal nitric oxide synthase: Evidence for two

identical highly anticooperative pteridine binding sites, *Biochemistry 35*, 16735−16745.
4. Griffith, O. W., and Stuehr, D. J. (1995) Nitric oxide synthases: Properties and catalytic mechanism, *Annu. Rev. Physiol. 57*, 707−736.
5. Bredt, D. S., and Snyder, S. H. (1990) Isolation of nitric oxide synthetase, a calmodulin-requiring enzyme, *Proc. Natl. Acad. Sci. U.S.A. 87*, 682−685.
6. Xie, Q. W., Cho, H. J., Calaycay, J., Mumford, R. A., Swiderek, K. M., Lee, T. D., Ding, A., Troso, T., and Nathan, C. (1992) Cloning and characterization of inducible nitric oxide synthase from mouse macrophages, *Science 256*, 225−228.
7. Pollock, J. S., Forstermann, U., Mitchell, J. A., Warner, T. D., Schmidt, H. H., Nakane, M., and Murad, F. (1991) Purification and characterization of particulate endothelium-derived relaxing factor synthase from cultured and native bovine aortic endothelial cells, *Proc. Natl. Acad. Sci. U.S.A. 88*, 10480−10484.
8. Stuehr, D. J. (1997) Structure−function aspects in the nitric oxide synthases, *Annu. Rev. Pharmacol. Toxicol. 37*, 339−359.
9. Masters, B. S., McMillan, K., Sheta, E. A., Nishimura, J. S., Roman, L. J., and Martasek, P. (1996) Neuronal nitric oxide synthase, a modular enzyme formed by convergent evolution: Structure studies of a cysteine thiolate-liganded heme protein that hydroxylates L-arginine to produce NO, *FASEB J. 10*, 552−558.
10. Stuehr, D. J. (1999) Mammalian nitric oxide synthases, *Biochim. Biophys. Acta 1411*, 217−230.
11. Mayer, B., and Hemmens, B. (1997) Biosynthesis and action of nitric oxide in mammalian cells, *Trends Biochem. Sci. 22*, 477−481.
12. Crane, B. R., Arvai, A. S., Ghosh, D. K., Wu, C., Getzoff, E. D., Stuehr, D. J., and Tainer, J. A. (1998) Structure of nitric oxide synthase oxygenase dimer with pterin and substrate, *Science 279*, 2121−2126.
13. Fischmann, T. O., Hruza, A., Niu, X. D., Fossetta, J. D., Lunn, C. A., Dolphin, E., Prongay, A. J., Reichert, P., Lundell, D. J., Narula, S. K., and Weber, P. C. (1999) Structural characterization of nitric oxide synthase isoforms reveals striking active-site conservation, *Nat. Struct. Biol. 6*, 233−242.
14. Sheta, E. A., McMillan, K., and Masters, B. S. (1994) Evidence for a bidomain structure of constitutive cerebellar nitric oxide synthase, *J. Biol. Chem. 269*, 15147−15153.
15. Gachhui, R., Presta, A., Bentley, D. F., Abu-Soud, H. M., McArthur, R., Brudvig, G., Ghosh, D. K., and Stuehr, D. J. (1996) Characterization of the reductase domain of rat neuronal nitric oxide synthase generated in the methylotrophic yeast *Pichia pastoris*. Calmodulin response is complete within the reductase domain itself, *J. Biol. Chem. 271*, 20594−20602.
16. Garcin, E. D., Bruns, C. M., Lloyd, S. J., Hosfield, D. J., Tiso, M., Gachhui, R., Stuehr, D. J., Tainer, J. A., and Getzoff, E. D. (2004) Structural basis for isozyme-specific regulation of electron transfer in nitric-oxide synthase, *J. Biol. Chem. 279*, 37918−37927.
17. Wang, Z. Q., Wei, C. C., and Stuehr, D. J. (2002) A conserved tryptophan 457 modulates the kinetics and extent of N-hydroxy-L-arginine oxidation by inducible nitric-oxide synthase, *J. Biol. Chem. 277*, 12830−12837.
18. Wei, C. C., Wang, Z. Q., Wang, Q., Meade, A. L., Hemann, C., Hille, R., and Stuehr, D. J. (2001) Rapid kinetic studies link tetrahydrobiopterin radical formation to heme-dioxy reduction and arginine hydroxylation in inducible nitric-oxide synthase, *J. Biol. Chem. 276*, 315−319.
19. Ledbetter, A. P., McMillan, K., Roman, L. J., Masters, B. S., Dawson, J. H., and Sono, M. (1999) Low-temperature stabilization and spectroscopic characterization of the dioxygen complex of the ferrous neuronal nitric oxide synthase oxygenase domain, *Biochemistry 38*, 8014−8021.
20. Abu-Soud, H. M., Gachhui, R., Raushel, F. M., and Stuehr, D. J. (1997) The ferrous-dioxy complex of neuronal nitric oxide synthase. Divergent effects of L-arginine and tetrahydrobiopterin on its stability, *J. Biol. Chem. 272*, 17349−17353.
21. Rusche, K. M., Spiering, M. M., and Marletta, M. A. (1998) Reactions catalyzed by tetrahydrobiopterin-free nitric oxide synthase, *Biochemistry 37*, 15503−15512.
22. Mayer, B., Wu, C., Gorren, A. C., Pfeiffer, S., Schmidt, K., Clark, P., Stuehr, D. J., and Werner, E. R. (1997) Tetrahydrobiopterin binding to macrophage inducible nitric oxide synthase: Heme spin shift and dimer stabilization by the potent pterin antagonist 4-amino-tetrahydrobiopterin, *Biochemistry 36*, 8422−8427.
23. Sorlie, M., Gorren, A. C., Marchal, S., Shimizu, T., Lange, R., Andersson, K. K., and Mayer, B. (2003) Single-turnover of nitric-oxide synthase in the presence of 4-amino-tetrahydrobiopterin: Proposed role for tetrahydrobiopterin as a proton donor, *J. Biol. Chem. 278*, 48602−48610.
24. Wei, C. C., Wang, Z. Q., Hemann, C., Hille, R., and Stuehr, D. J. (2003) A tetrahydrobiopterin radical forms and then becomes reduced during N^{ω}-hydroxyarginine oxidation by nitric-oxide synthase, *J. Biol. Chem. 278*, 46668−46673.
25. Raman, C. S., Li, H., Martasek, P., Kral, V., Masters, B. S., and Poulos, T. L. (1998) Crystal structure of constitutive endothelial nitric oxide synthase: A paradigm for pterin function involving a novel metal center, *Cell 95*, 939−950.
26. Crane, B. R., Arvai, A. S., Ghosh, S., Getzoff, E. D., Stuehr, D. J., and Tainer, J. A. (2000) Structures of the N^{ω}-hydroxy-L-arginine complex of inducible nitric oxide synthase oxygenase dimer with active and inactive pterins, *Biochemistry 39*, 4608−4621.
27. Aoyagi, M., Arvai, A. S., Ghosh, S., Stuehr, D. J., Tainer, J. A., and Getzoff, E. D. (2001) Structures of tetrahydrobiopterin binding-site mutants of inducible nitric oxide synthase oxygenase dimer and implicated roles of Trp457, *Biochemistry 40*, 12826−12832.
28. Ghosh, S., Wolan, D., Adak, S., Crane, B. R., Kwon, N. S., Tainer, J. A., Getzoff, E. D., and Stuehr, D. J. (1999) Mutational analysis of the tetrahydrobiopterin-binding site in inducible nitric-oxide synthase, *J. Biol. Chem. 274*, 24100−24112.
29. Sagami, I., Sato, Y., Daff, S., and Shimizu, T. (2000) Aromatic residues and neighboring Arg414 in the (6*R*)-5,6,7,8-tetrahydro-L-biopterin binding site of full-length neuronal nitric-oxide synthase are crucial in catalysis and heme reduction with NADPH, *J. Biol. Chem. 275*, 26150−26157.
30. Wang, Z. Q., Wei, C. C., Ghosh, S., Meade, A. L., Hemann, C., Hille, R., and Stuehr, D. J. (2001) A conserved tryptophan in nitric oxide synthase regulates heme-dioxy reduction by tetrahydrobiopterin, *Biochemistry 40*, 12819−12825.
31. Abu-Soud, H. M., Wang, J., Rousseau, D. L., Fukuto, J. M., Ignarro, L. J., and Stuehr, D. J. (1995) Neuronal nitric oxide synthase self-inactivates by forming a ferrous-nitrosyl complex during aerobic catalysis, *J. Biol. Chem. 270*, 22997−23006.
32. Sambrook, J., and Russell, D. W. (2004) *Molecuar Cloning, A Laboratory Manual*, Cold Spring Harbor Laboratory Press, Plainview, NY.
33. Gachhui, R., Ghosh, D. K., Wu, C., Parkinson, J., Crane, B. R., and Stuehr, D. J. (1997) Mutagenesis of acidic residues in the oxygenase domain of inducible nitric-oxide synthase identifies a glutamate involved in arginine binding, *Biochemistry 36*, 5097−5103.
34. Stuehr, D. J., and Ikeda-Saito, M. (1992) Spectral characterization of brain and macrophage nitric oxide synthases. Cytochrome P-450-like hemeproteins that contain a flavin semiquinone radical, *J. Biol. Chem. 267*, 20547−20550.
35. Ghosh, D. K., Wu, C., Pitters, E., Moloney, M., Werner, E. R., Mayer, B., and Stuehr, D. J. (1997) Characterization of the inducible nitric oxide synthase oxygenase domain identifies a 49 amino acid segment required for subunit dimerization and tetrahydrobiopterin interaction, *Biochemistry 36*, 10609−10619.
36. Panda, K., Ghosh, S., and Stuehr, D. J. (2001) Calmodulin activates intersubunit electron transfer in the neuronal nitric-oxide synthase dimmer, *J. Biol. Chem. 276*, 23349−23356.
37. Adak, S., Aulak, K. S., and Stuehr, D. J. (2001) Chimeras of nitric-oxide synthase types I and III establish fundamental correlates between heme reduction, heme-NO complex formation, and catalytic activity, *J. Biol. Chem. 276*, 23246−23252.
38. Abu-Soud, H. M., Ichimori, K., Nakazawa, H., and Stuehr, D. J. (2001) Regulation of inducible nitric oxide synthase by self-generated NO, *Biochemistry 40*, 6876−6881.
39. Adak, S., Wang, Q., and Stuehr, D. J. (2000) Molecular basis for hyperactivity in tryptophan 409 mutants of neuronal NO synthase, *J. Biol. Chem. 275*, 17434−17439.
40. Wang, Z. Q., Wei, C. C., Sharma, M., Pant, K., Crane, B. R., and Stuehr, D. J. (2004) A conserved Val to Ile switch near the heme pocket of animal and bacterial nitric-oxide synthases helps determine their distinct catalytic profiles, *J. Biol. Chem. 279*, 19018−19025.
41. Santolini, J., Meade, A. L., and Stuehr, D. J. (2001) Differences in three kinetic parameters underpin the unique catalytic profiles of nitric-oxide synthases I, II, and III, *J. Biol. Chem. 276*, 48887−48898.

42. Panda, K., Adak, S., Aulak, K. S., Santolini, J., McDonald, J. F., and Stuehr, D. J. (2003) Distinct influence of N-terminal elements on neuronal nitric-oxide synthase structure and catalysis, *J. Biol. Chem. 278*, 37122−37131.
43. Abu-Soud, H. M., Wang, J., Rousseau, D. L., and Stuehr, D. J. (1999) Stopped-flow analysis of substrate binding to neuronal nitric oxide synthase, *Biochemistry 38*, 12446−12451.
44. Ghosh, D. K., Wu, C., Pitters, E., Moloney, M., Werner, E. R., Mayer, B., and Stuehr, D. J. (1997) Characterization of the inducible nitric oxide synthase oxygenase domain identifies a 49 amino acid segment required for subunit dimerization and tetrahydrobiopterin interaction, *Biochemistry 36*, 10609−10619.
45. McMillan, K., and Masters, B. S. (1993) Optical difference spectrophotometry as a probe of rat brain nitric oxide synthase heme-substrate interaction, *Biochemistry 32*, 9875−9880.
46. Gorren, A. C., and Mayer, B. (2002) Tetrahydrobiopterin in nitric oxide synthesis: A novel biological role for pteridines, *Curr. Drug Metab. 3*, 133−157.
47. Marletta, M. A., Hurshman, A. R., and Rusche, K. M. (1998) Catalysis by nitric oxide synthase, *Curr. Opin. Chem. Biol. 2*, 656−663.
48. Adak, S., Sharma, M., Meade, A. L., and Stuehr, D. J. (2002) A conserved flavin-shielding residue regulates NO synthase electron transfer and nicotinamide coenzyme specificity, *Proc. Natl. Acad. Sci. U.S.A. 99*, 13516−13521.
49. Adak, S., and Stuehr, D. J. (2001) A proximal tryptophan in NO synthase controls activity by a novel mechanism, *J. Inorg. Biochem. 83*, 301−308.
50. Presta, A., Weber-Main, A. M., Stankovich, M. T., and Stuehr, D. J. (1998) Comparative Effects of Substrates and Pterin Cofactor on the Heme Midpoint Potential in Inducible and Neuronal Nitric Oxides Synthases, *J. Am. Chem. Soc. 120*, 9460−9465.
51. Adak, S., Santolini, J., Tikunova, S., Wang, Q., Johnson, J. D., and Stuehr, D. J. (2001) Neuronal nitric-oxide synthase mutant (Ser-1412 → Asp) demonstrates surprising connections between heme reduction, NO complex formation, and catalysis, *J. Biol. Chem. 276*, 1244−1252.
52. Stuehr, D. J., Santolini, J., Wang, Z. Q., Wei, C. C., and Adak, S. (2004) Update on mechanism and catalytic regulation in the NO synthases, *J. Biol. Chem. 279*, 36167−36170.
53. Boggs, S., Huang, L., and Stuehr, D. J. (2000) Formation and reactions of the heme-dioxygen intermediate in the first and second steps of nitric oxide synthesis as studied by stopped-flow spectroscopy under single-turnover conditions, *Biochemistry 39*, 2332−2339.
54. Wei, C. C., Crane, B. R., and Stuehr, D. J. (2003) Tetrahydrobiopterin radical enzymology, *Chem. Rev. 103*, 2365−2383.
55. Mayer, B., and Werner, E. R. (1995) Why tetrahydrobiopterin? *Adv. Pharmacol. 34*, 251−261.
56. Abu-Soud, H. M., Ichimori, K., Presta, A., and Stuehr, D. J. (2000) Electron transfer, oxygen binding, and nitric oxide feedback inhibition in endothelial nitric-oxide synthase, *J. Biol. Chem. 275*, 17349−17357.
57. Hurshman, A. R., Krebs, C., Edmondson, D. E., Huynh, B. H., and Marletta, M. A. (1999) Formation of a pterin radical in the reaction of the heme domain of inducible nitric oxide synthase with oxygen, *Biochemistry 38*, 15689−15696.
58. Bec, N., Gorren, A. F. C., Mayer, B., Schmidt, P. P., Andersson, K. K., and Lange, R. (2000) The role of tetrahydrobiopterin in the activation of oxygen by nitric-oxide synthase, *J. Inorg. Biochem. 81*, 207−211.
59. Gachhui, R., Abu-Soud, H. M., Ghosh, D. K., Presta, A., Blazing, M. A., Mayer, B., George, S. E., and Stuehr, D. J. (1998) Neuronal nitric-oxide synthase interaction with calmodulin-troponin C chimeras, *J. Biol. Chem. 273*, 5451−5454.
60. Berka, V., Yeh, H. C., Gao, D., Kiran, F., and Tsai, A. L. (2004) Redox function of tetrahydrobiopterin and effect of L-arginine on oxygen binding in endothelial nitric oxide synthase, *Biochemistry 43*, 13137−13148.
61. Stuehr, D., Pou, S., and Rosen, G. M. (2001) Oxygen reduction by nitric-oxide synthases, *J. Biol. Chem. 276*, 14533−14536.
62. Roman, L. J., Martasek, P., and Masters, B. S. (2002) Intrinsic and extrinsic modulation of nitric oxide synthase activity, *Chem. Rev. 102*, 1179−1190.
63. Jones, R. J., Smith, S. M., Gao, Y. T., DeMay, B. S., Mann, K. J., Salerno, K. M., and Salerno, J. C. (2004) The function of the small insertion in the hinge subdomain in the control of constitutive mammalian nitric-oxide synthases, *J. Biol. Chem. 279*, 36876−36883.
64. Li, D., Stuehr, D. J., Yeh, S. R., and Rousseau, D. L. (2004) Heme distortion modulated by ligand-protein interactions in inducible nitric-oxide synthase, *J. Biol. Chem. 279*, 26489−26499.
65. Santolini, J., Adak, S., Curran, C. M., and Stuehr, D. J. (2001) A kinetic simulation model that describes catalysis and regulation in nitric-oxide synthase, *J. Biol. Chem. 276*, 1233−1243.
66. Stuehr, D. J., Cho, H. J., Kwon, N. S., Weise, M. F., and Nathan, C. F. (1991) Purification and characterization of the cytokine-induced macrophage nitric oxide synthase: An FAD- and FMN-containing flavoprotein, *Proc. Natl. Acad. Sci. U.S.A. 88*, 7773−7777.

BI047508P